metals

MDPI

Article

Tensile Properties and Fracture Behavior of a Powder-Thixoformed 2024Al/SiC$_p$ Composite at Elevated Temperatures

Pubo Li and Tijun Chen *

State Key Laboratory of Advanced Processing and Recycling of Nonferrous Metals,
Lanzhou University of Technology, Lanzhou 730050, China; lipubogs@163.com
* Correspondence: chentj@lut.cn; Tel.: +86-931-297-6573

Received: 23 August 2017; Accepted: 28 September 2017; Published: 1 October 2017

Abstract: In the present work, the tensile properties and fracture behavior of a 2024Al composite reinforced with 10 vol % SiC$_p$ and fabricated via powder thixoforming (PT) were studied at temperatures ranging from 25 °C to 300 °C with a strain rate of 0.05 s^{-1}, as well as the PT 2024 alloy. The results indicated that the tensile strengths of both the PT materials were all decreased with increasing the temperature, but the decrease rate of the composite was smaller than that of the 2024 alloy, and the composite exhibited higher tensile strength than that of the 2024 alloy at all of the employed testing temperatures due to the strengthening role of SiC$_p$. Increasing temperature was beneficial for enhancing the ductility of materials, and the maximum elongation was reached at 250 °C. The elongation decrease over 250 °C was attributed to the cavity formation due to the debonding of the SiC$_p$/Al interface and the fracturing of the matrix between SiC$_p$. The fracture of the composite at room temperature initiated from the fracture of SiC$_p$ and the debonding of the SiC$_p$/Al interface, but that at high temperatures was dominated by void nucleation and growth in the matrix besides the interface debonding.

Keywords: powder thixoforming; composite; high temperature; tensile properties; fracture

---

1. Introduction

Owing to their low density, high specific strength and stiffness, good wear resistance, and good thermal and electrical properties, aluminum alloy matrix composites reinforced with SiC particles (Al/SiC$_p$ composites) have attracted increasing attention in the fields of aerospace, automotive, military, electronics, and sports [1–4]. Among the many fabricating methods, powder metallurgy (PM) is the most promising route because of the uniform distribution of SiC$_p$, controlled SiC$_p$/Al interface, and flexible design of constituents [5,6]. However, the wide application of PM is largely limited by some challenges such as high production cost and great difficulty in synthesizing components with complex shapes and compact microstructures [7]. However, thixoforming is just appropriate for producing components with such characteristics [8,9]. The authors combined the merits of these two technologies and proposed a new fabrication method of powder thixoforming (PT) [10]. For this method, a green composite compact is first prepared by using the mixing and cold pressing steps of PM. Then a PT composite component is fabricated via partial remelting and subsequent thixoforming.

So far, various aspects of Al/SiC$_p$ composites fabricated via PM have been studied extensively, especially in terms of the mechanical properties at room temperature and elevated temperatures. For example, Angers et al. studied the effects of SiC$_p$ volume fraction and milling time on the microstructure and mechanical properties of 2024Al/SiC$_p$ composite prepared by PM [11], and Xiao et al. reported the effects of testing temperature and strain rate on hot deformation characteristics of a 2009Al/SiC$_p$ composite fabricated by PM [12]. Our previous studies revealed that the microstructures of the PT materials were significantly different from those fabricated by PM [10,13]. Hence, the resulting tensile properties and corresponding fracture behavior will also differ from those prepared by PM. PT is a novel processing method, and the previous studies focused only on the semisolid microstructural evolution during partial remelting and the effects of processing parameters (such as the mold temperature, reheating temperature and time, and volume fraction of reinforcements) on the microstructure and room-temperature mechanical properties of the resulting Al/SiC$_p$ composites [10,14–16]. Additionally, the effect of solution heat treatment has also been investigated [17]. The experimental results revealed that the Al/SiC$_p$ composites with excellent mechanical properties could be fabricated using PT. Unfortunately, there has been no study on the elevated temperature mechanical properties of the PT Al/SiC$_p$ composites.

Therefore, in this work, a 2024Al matrix composite reinforced with 10 vol % SiC$_p$ was successfully fabricated via PT route and its mechanical properties, strengthening mechanisms, and the corresponding tensile fracture behavior in a temperature range from 25 °C (room temperature) to 300 °C were investigated.

2. Materials and Methods

The matrix alloy used in present work was gas-atomized 2024Al powders, and the chemical composition (in wt %) was 4.22Cu, 1.35Mg, 0.5Si, and the balance Al. The SiC particles (SiC$_p$) were used as reinforcements. Figure 1 indicates that the morphologies of the SiC$_p$ and Al$_p$ were angular and spheroidal, respectively. The average size of the 2024Al powders was 20 µm, and that of the SiC$_p$ was 15 µm (Figure 2). To enhance the wettability between the matrix alloy and SiC$_p$ as well as to avoid the formation of undesired interfacial reaction products that were always detrimental to the mechanical properties of the composites, the SiC$_p$ have been oxidized at 930 °C for 5 h prior to incorporation into the 2024Al powders.

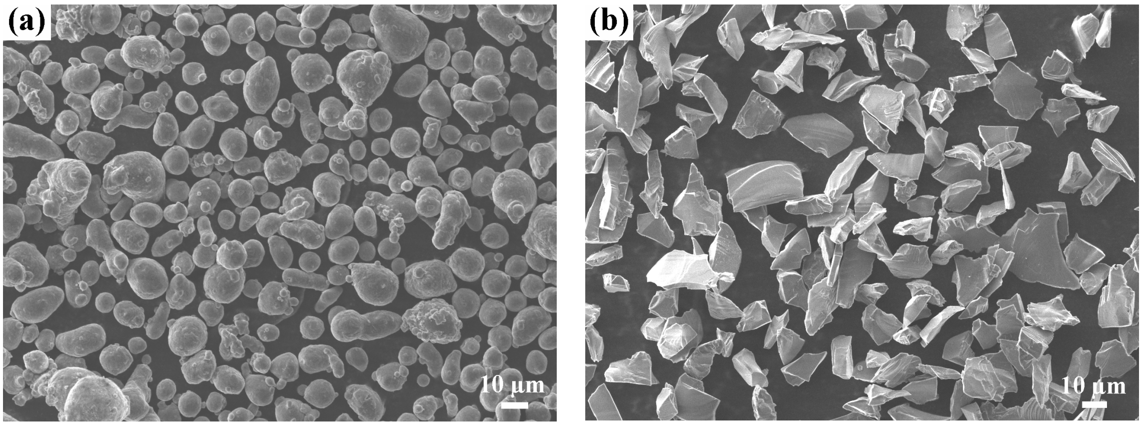

Figure 1. Morphologies of (**a**) 2024Al powders and (**b**) SiC$_p$.

The preparation of the 2024Al/SiC$_p$ composite by PT mainly includes four procedures. First, the 2024 powders were blended with the oxidized SiC$_p$ by a ND7-21 planetary ball mill (Nanjing Levinstep Technology Co., Ltd., Nanjing, China). The ball milling time, ball-to-powder weight ratio, and rotation speed were maintained at 30 min, 5:1, and 100 r/min, respectively. Second, the mixed powders were compacted into green composite compacts with dimensions of Φ45 mm × 20 mm. Subsequently, the green compacts were partially remelted to obtain semisolid ingots. Finally, the semisolid ingots were thixoformed, and some composite products with 50 mm of diameter and 16 mm of thickness were fabricated. The detailed processing procedures have been reported in our previous studies [16,18]. For comparison, some PT 2024 alloy components were fabricated by pressing of the as-received 2024 powders, partial remelting, and subsequent thixoforming processes.

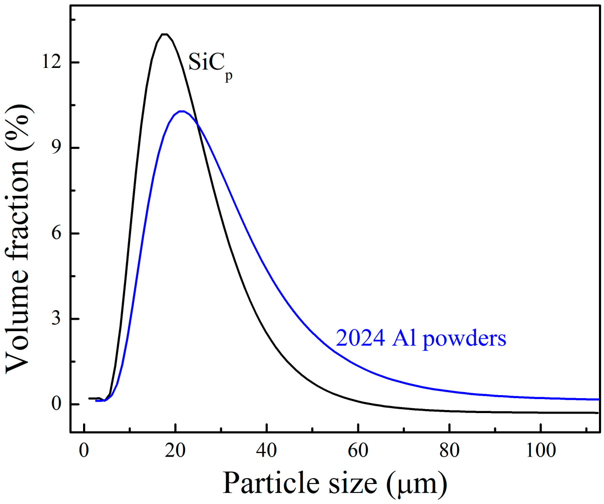

Figure 2. Size distributions of the 2024Al powders and SiC$_p$.

Tensile specimens, as illustrated in Figure 3, were machined from the center region of each product parallel to the direction of the applied pressure. Tensile tests were performed using a WDW-100D universal material testing machine (Jinan HengXu Testing Machine Technology Co., Ltd., Jinan, China) equipped with a heating furnace. The specimens were held at the testing temperatures for 10 min before loading in order to achieve a uniform temperature in the specimens. Tests were carried out at 25 °C (room temperature), 100 °C, 150 °C, 200 °C, 250 °C, and 300 °C, respectively, with a strain rate of 0.05 s^{-1}. The fractured samples were quickly water-quenched to preserve the deformed microstructures. Three tensile specimens were tested for each temperature. The fracture surfaces were observed using a QUANTA FEG 450 scanning electron microscope (SEM, FEI, Hillsboro, OR, USA) and analyzed by energy dispersive X-ray spectroscopy (EDS, FEI, Hillsboro, OR, USA). The side views of the typical fracture surfaces were examined by the SEM to clarify the fracture mechanisms at different testing temperatures. To study the effect of the testing temperature on the strengthening mechanisms, the dislocation density was calculated using D8 ADVANCE X-ray diffraction (XRD, Rigaku, Tokyo, Japan). The microstructure prior to tensile testing was also carried out, and the dimensions of the metallographic specimens are 10 mm × 10 mm × 16 mm. To quantitatively examine the primary particle size and eutectic θ-phase concentration, the related SEM images were analyzed by Image-Pro Plus 5.0 software (Media Cybernetics Company, Silver Spring, MD, USA). At least three SEM images were examined.

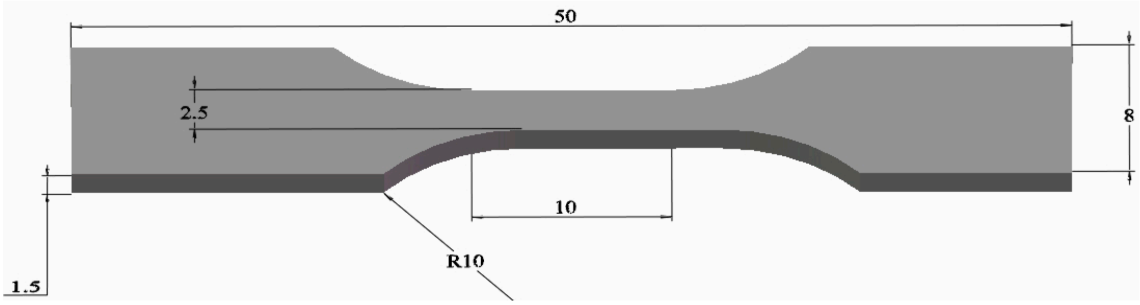

Figure 3. Dimensions of the tensile testing specimen (unit: mm).

3. Results and Discussion

3.1. Microstructure of the As-Fabricated 2024Al/SiC$_p$ Composite

Figure 4 shows the microstructures of the thixoformed 2024Al/SiC$_p$ composite and the 2024 alloy, respectively. The microstructure of the 2024Al/SiC$_p$ composite consisted of fine spheroidal primary α-Al particles (indicated by the arrows A in Figure 4a), intergranular secondary solidified structures (SSS) (indicated by the arrows B in Figure 4a), and SiC$_p$ that distributed homogeneously within SSS (indicated by the arrows Figure 4a), which is different from the coarsened microstructures produced by conventional processes [19,20]. The microstructure of the 2024 alloy was similar to that of the composite in addition to the SiC$_p$ (Figure 4c). The SSS in these two materials included the secondary α-Al phases (indicated by the arrows C in Figure 4b), eutectic α-Al phase (indicated by the arrows D in Figure 4b), and eutectic θ-phase (indicated by the arrows E in Figure 4b). It can be found that the primary particle size (24.02 µm) and eutectic θ-phase concentration (4.34%) of the composite was smaller and less than those (34.05 µm and 5.15%) of the alloy, respectively (comparing Figure 4b,d).

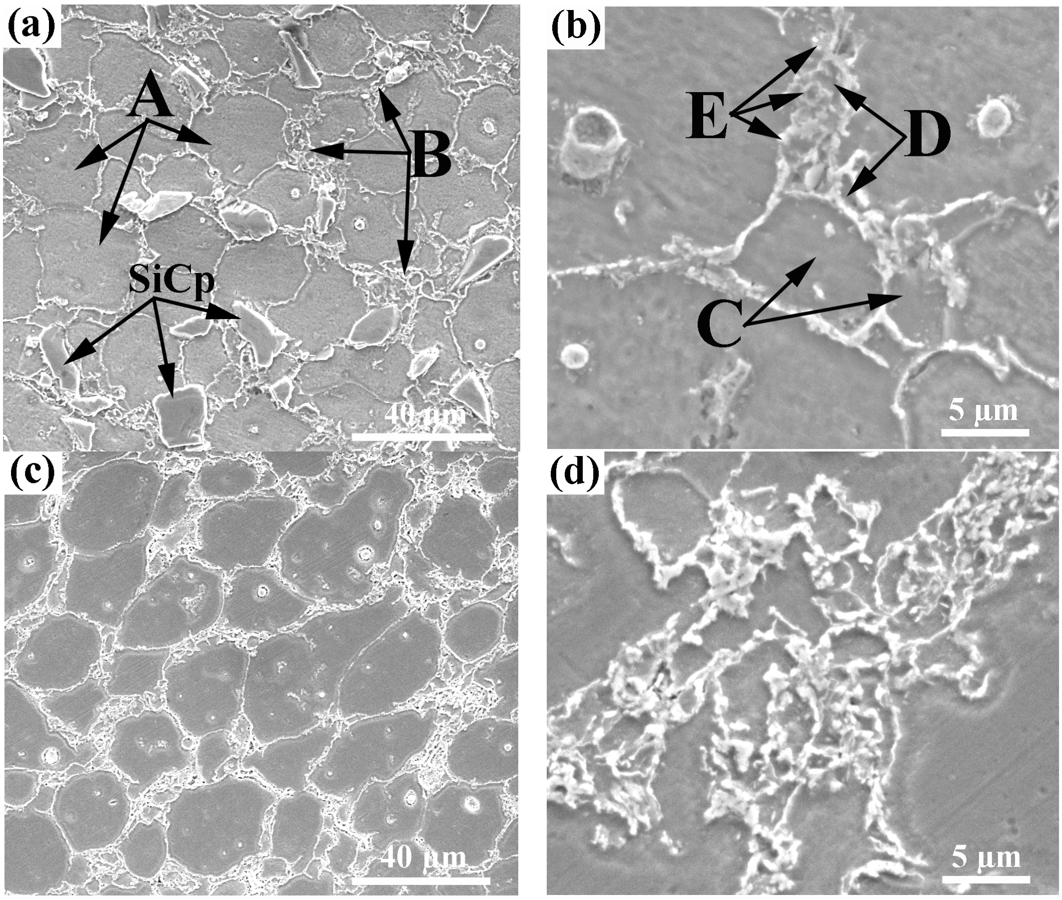

Figure 4. SEM micrographs of (**a**,**b**) 2024Al/SiC$_p$ composite and (**c**,**d**) 2024 alloy.

The mechanisms for thixoformed microstructure have been detailedly clarified in our previous investigations [21]. In short, the secondary α-Al phases preferentially attached to the surfaces of the primary α-Al phase, and then the equiaxed secondary α-Al phases nucleated in the regions far away from the primary particles upon achieving the requirements for heterogeneous nucleation. Finally, solidification was completed through the eutectic reaction of the residual liquid phase. It should be noted that the incorporation of SiC$_p$ into the 2024 alloy decreased the coarsening rate [18], thereby the primary particle size was smaller than that of the 2024 alloy. The uniform distribution of SiC$_p$ within the Al powders was achieved by ball mill procedure, and the eutectics partially dissolved towards the primary α-Al phase during ball milling because of the increased mixture temperature caused by ball-powder collision and ball-ball sliding [22], lowering the eutectic concentration of the milled Al powders compared with that of the as-received 2024 powders. Moreover, the ball-milled Al powders always possessed high-density dislocations due to the plastic deformation that occurred during ball milling [23], providing convenient channels for dissolution of θ phase during partial remelting. Besides, the effective liquid fraction of the composite was less than that of the 2024 alloy because of the SiC_p incorporation, decreasing the eutectic concentration. Therefore, the primary particle size was smaller and eutectic θ-phase concentration was less compared with the PT alloy. From this standpoint, the generation of the powder-thixoformed microstructures can be well interpreted.

3.2. Effect of Temperature on Tensile Properties and Strengthening Mechanisms

Figure 5 shows the variations of tensile properties of the 2024Al/SiC_p composite with the testing temperature, as well as the 2024 alloy. It was observed that the composite tested at room temperature had an ultimate tensile strength (UTS) of 388 MPa and 0.2% offset yield strength (YS) of 297 MPa, increased by 29.3% and 35.0%, respectively, compared to those of the 2024 alloy. In addition, both the UTS and YS were all obviously higher than those of the congeneric 2024Al/SiC_p composites prepared by other methods. For example, the UTS and YS of the 10 vol % 10 μm SiC_p reinforced 2024 composite prepared by extrusion were 308 MPa and 210 MPa, respectively [24], and those of the 15 vol % 10 μm SiC_p reinforced 2024 composite prepared by PM were 320 MPa and 212 MPa, respectively [25]. Furthermore, these two properties of the PT 2024 alloy were also significantly higher than those of the squeeze-cast 2024 alloy [26]. All of these show that PT is a promising method to fabricate metallic materials, especially the particle reinforced metal matrix composites. As the testing temperature increased, decreases in the UTS and YS of both the composite and alloy were attained, but the UTS and YS of the composite were always higher than those of the 2024 alloy within the entire range of testing temperatures. Especially, the decrease rate of the composite was obviously slower than that of the alloy within 25 °C–150 °C. The UTS and YS of the composite were only decreased by 18.8% and 21.9% at 150 °C, while those of the 2024 alloy were decreased by 24.3% and 25.9%. That is, the composite exhibited better strength stability against temperature over the 2024 alloy. As expected, the elongation of the composite increased continuously as the temperature increased, but it slightly decreased when the testing temperature exceeded 250 °C. However, the elongation of the 2024 alloy always increased in the entire temperature range. In addition, the elongation of the composite was much lower than that of the alloy at each testing temperature, lowered by 63.5% and 24.4% compared with the 2024 alloy at 25 °C and 300 °C, respectively.

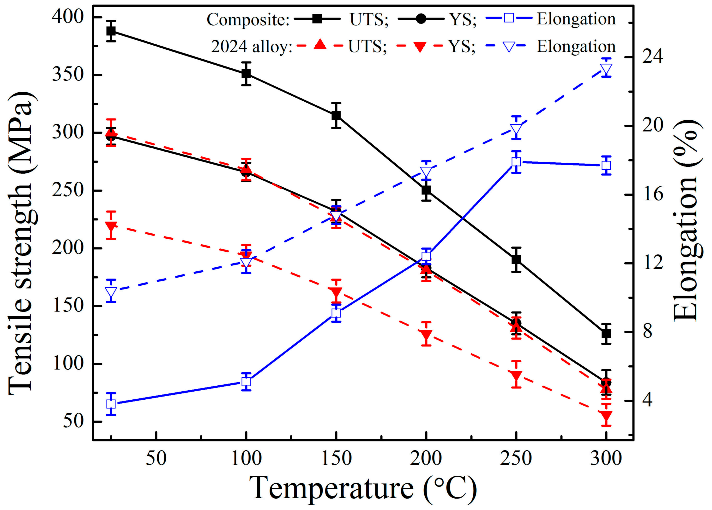

Figure 5. Variations of the mechanical properties with the testing temperature.

It is known that two types of the strengthening mechanisms were responsible for the enhanced strength in the composite over the unreinforced matrix alloy: direct and indirect strengthening [27–30]. The direct strengthening operated by load transfer from the matrix to the reinforcements. The indirect strengthening resulted from the microstructural changes of the composite, such as thermal mismatch strengthening (TMS) and geometrically necessary dislocations strengthening (GNDs).

According to the load-transfer strengthening (LTS) theory, the YS increment, $\Delta\sigma_{\mathrm{LTS}}$, was given by [27]:

$$\Delta\sigma_{\mathrm{LTS}} = 0.5V_{\mathrm{c}}\sigma_{\mathrm{m}} \tag{1}$$

where σ_{m} and V_{c} are the matrix YS and volume fraction of $\mathrm{SiC_p}$, respectively.

The YS increment induced by TMS, $\Delta\sigma_{\mathrm{TMS}}$, was given by [29]:

$$\Delta\sigma_{\mathrm{TMS}} = \sqrt{3}BG_{\mathrm{m}}b\sqrt{12V_{\mathrm{c}}\Delta\alpha\Delta T/(bd_{\mathrm{c}} - bd_{\mathrm{c}}V_{\mathrm{c}})} \tag{2}$$

where B is dislocation strengthening coefficient with a value of 1.25, G_{m} is the shear modulus (26.4 GPa), $\Delta\alpha$ is the mismatch in CTE between the matrix and $\mathrm{SiC_p}$ ($19.1 \times 10^{-6}\ \mathrm{K}^{-1}$), ΔT is the difference between the processing temperature and testing temperature (ΔT = 600 K), d_{c} is the average size of the $\mathrm{SiC_p}$, and b is the Burgers vector (0.286 nm) [31–33].

The YS increment, $\Delta\sigma_{\mathrm{GNDS}}$, can be calculated according to [30]:

$$\Delta\sigma_{\mathrm{GNDS}} = 2G_{\mathrm{m}}V_{\mathrm{c}}\varepsilon_{\mathrm{c}}(1-v)/(1-2v) \tag{3}$$

where v is Poisson's ratio (0.33), and ε_{c} is yield strain (0.2%).

The contributions of LTS, TMS, and GNDs to YS increments calculating from Equations (1)–(3) were 11.0 MPa, 30.9 MPa, and 20.8 MPa, respectively. Ramakrishnan reported that both the additive and synergistic effects of different strengthening effects should be taken into account if several kinds of strengthening mechanisms operate simultaneously [34], and thus the YS of the composite can be predicted by superposing the individual contribution of the aforementioned strengthening mechanisms. The predicted results indicated that the calculated value is much closer to the experimental value of the composite (Figure 6), which quantitatively demonstrated that the load-transfer strengthening and dislocation strengthening contributed to strengthening the composite at room temperature.

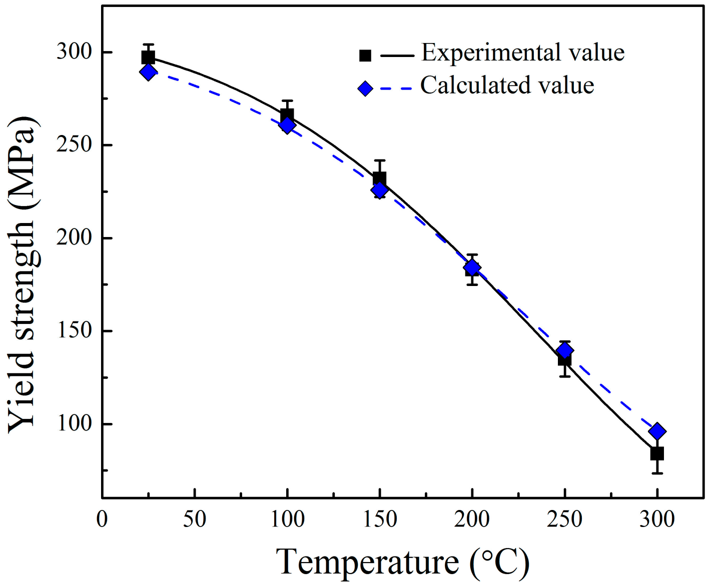

Figure 6. Comparison between theoretical calculation and experimental results.

Both the calculated YS and experimental YS of the composite decreased as the testing temperature increased (Figures 5 and 6), implying that the strengthening efficiency may increasingly become less effective. Dislocation strengthening was significantly dependent on the density of dislocations. To determine the strengthening contribution with temperature, the dislocation density was quantitatively calculate by XRD based on the broadening of the diffraction peaks. Figure 7a shows that XRD patterns of the composite tested at different temperatures, indicating that the full width at half maximum (W_{hkl}) values of the diffraction peaks decreased as the temperature increased. According to the Williamson-Hall equation (WH), W_{hkl} can be calculated with Equation (4) [35,36]:

$$W_{hkl} \cos \theta_{hkl} = \lambda / d + 4\varepsilon \sin \theta_{hkl} \tag{4}$$

where θ_{hkl} is the Bragg angle, λ is the wavelength (0.15406 nm), d is the crystallite size, and ε is the lattice strain. Plotting $W_{hkl} \cos\theta_{hkl}$ as a function of $4\sin\theta_{hkl}$ by performing linear regression analysis (Figure 7b), the ε and d values were determined by the slopes and intercepts of the fitted curves, respectively. The dislocation density, ρ, was given by Equation (5) [37]:

$$\rho = 2\sqrt{3}\varepsilon / (db) \tag{5}$$

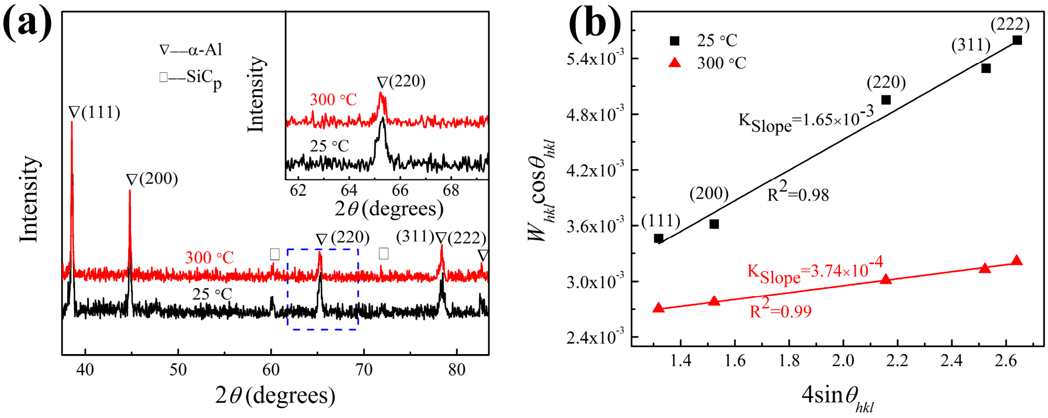

Figure 7. (**a**) XRD patterns and (**b**) Williamson-Hall (WH) plots of the composite tested at different temperatures.

For the composite tested at 25 °C and 300 °C, the values of ρ decreased from 1.6×10^{14} m^{-2} to 6.5×10^{13} m^{-2} as calculated from Equation (5). Increasing deformation temperature promoted dislocation motion by enhancing dislocation cross slip and climb due to the high thermal activation effect, and thus decreasing the dislocation density. It has been generally accepted that the strengthening contribution from dislocations, $\Delta\sigma_{\text{dis}}$, was calculated with the Bailey-Hirsch equation [38]:

$$\Delta\sigma_{\text{dis}} = M\beta G_{\text{m}} b\sqrt{\rho} \tag{6}$$

where M is the mean orientation factor (3.06) and β is a coefficient (0.2) [39]. Substituting Equation (5) into Equation (6), $\Delta\sigma_{\text{dis}}$ decreased from 58.4 MPa to 37.3 MPa with increasing the temperature from 25 °C to 300 °C, which quantitatively indicated that decreasing the dislocation density weakened the strength of the materials. Therefore, high temperature impeded the contribution of dislocation strengthening to YS increment.

On the basis of Equation (1), $\Delta\sigma_{\text{lt}}$ decreased from 11 MPa to 2.8 MPa when the temperature increased from 25 °C to 300 °C, which confirmed that high temperature degraded the load-transfer strengthening. During the tensile tests, the stress concentration around the SiC$_{\text{p}}$ was formed. The SiC$_{\text{p}}$/Al interfaces debonded and SiC$_{\text{p}}$ cracked when the stress concentration exceeded a certain level, as evidenced by Figure 8a that many cracked and debonded SiC_p distributed homogeneously on the resulting fracture surface. The SiC_p failure well verified that the SiC_p could effectively bear the external load transferred from the matrix during the tensile tests. That is, the contribution of load-transfer strengthening to YS increment at room temperature was operative. As the temperature increased, the void nucleation in the matrix has become more extensive, and cracks preferentially initiated in and propagated along the matrix, giving rise to the premature fracturing of the composite before the load-carrying capacity of SiC_p was operated completely. This can be demonstrated by the following experimental results shown in Section 3.3. Therefore, the load-transfer strengthening to YS increment of the composite tested at elevated temperature was lower than that at room temperature. From the aforementioned standpoints, the variations of mechanical properties with respect to the testing temperature can be well interpreted.

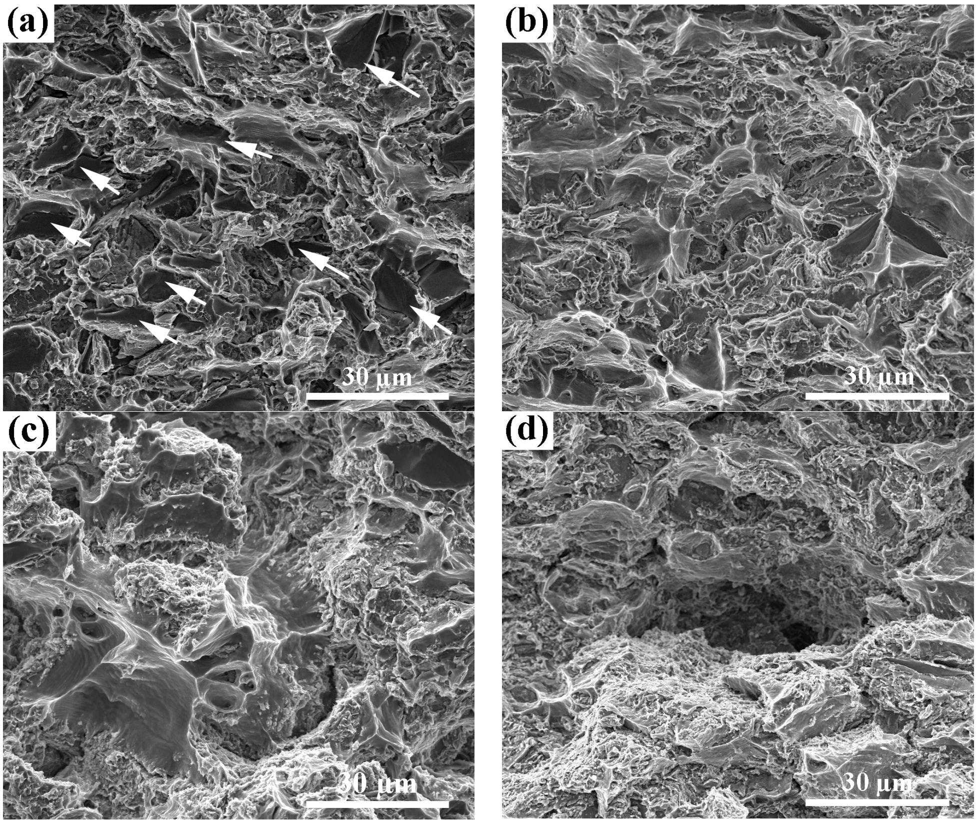

Figure 8. Fractographsof the composite tested at temperatures of (**a**) 25 °C; (**b**) 200 °C; (**c**) 250 °C; and (**d**) 300 °C.

3.3. Effect of Temperature on Tensile Fracture Behavior

The fracture surfaces of the 2024Al/SiC_p composite tested at different temperatures were shown in Figure 8. The fracture of the composite was found to be brittle at room temperature, as evidenced by the quasi-cleavage facets on the fracture surface (Figure 8a). Many failed SiC_p (including the cracked SiC_p and debonded SiC_p/Al interface) can also be observed (indicated by the arrows in Figure 8a). The primary α-Al particles basically maintained their original spheroidal morphology in the side view of fracture surface (comparing Figures 4a and 9a), which implies that no obvious plastic deformation occurred prior to fracture, and thus the ductility of composite was quite low. The visible SiC_p can also be observed in the side view of the fracture surface (Figure 9a). During the tensile tests, a higher stress concentration will be generated surrounding the SiC_p/Al interface due to the mismatch between the plastic deformation abilities of the SiC_p (only elastic deformation) and Al matrix (plastic deformation), which induces the cracking or debonding of the SiC_p if the concentrated stress reaches a critical value.

The failed SiC_p increased the points of crack initiation and propagation, and thus resulted in the premature fracture of the composite with a lower elongation. This has been evidenced by the in situ tensile testing in our previous work [16]. That is, the fracture of the composite at room temperature was mainly initiated from the fractured SiC_p and debonded SiC_p/Al interface. However, a large number of small dimples distributed homogeneously in the fracture surface of the 2024 alloy as shown in Figure 10a, indicating a ductile fracture mode.

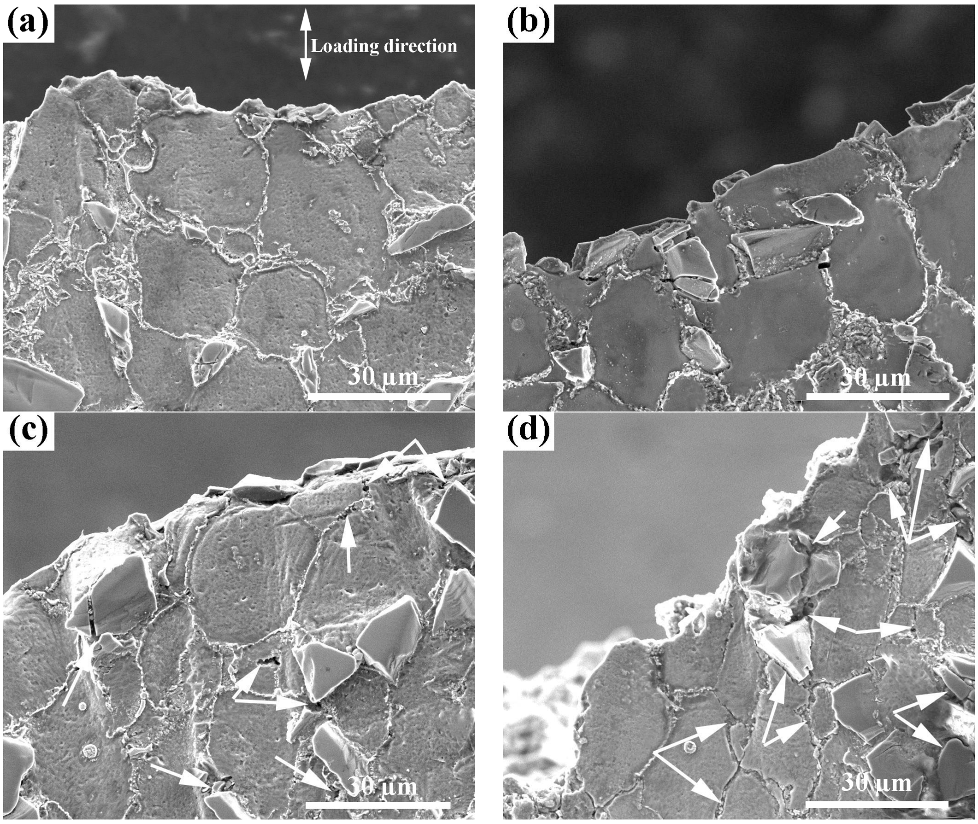

Figure 9. Side views of fracture surfaces of the composite tested at temperatures of (**a**) 25 °C; (**b**) 200 °C; (**c**) 250 °C; and (**d**) 300 °C.

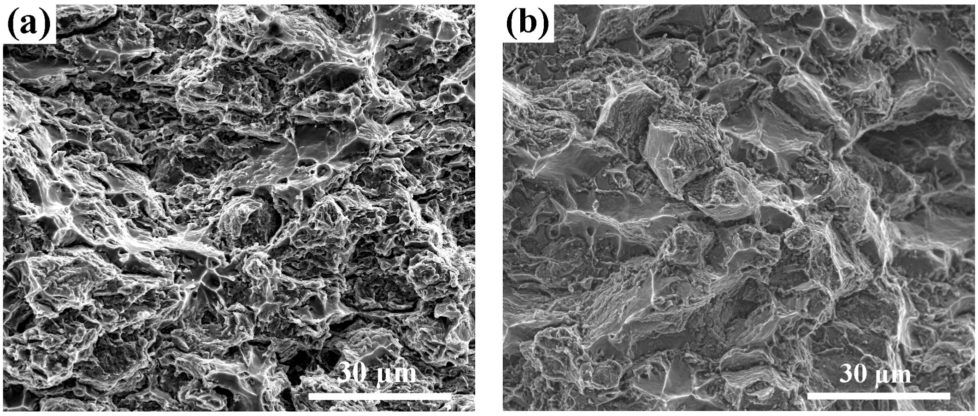

Figure 10. Fractographs of the 2024 alloy tested at temperatures of (**a**) 25 °C and (**b**) 300 °C.

When the composite was tested at 200 °C, the fracture surface was characterized by tear ridges, and shallow and small dimples was observed in some local regions (Figure 8b), which was indicative of a ductile–brittle mixed fracture mode.As the temperature exceeded 200 °C, the fracture surfaces were characterized by large pits and heaves (Figure 8c,d and Figure 10b), indicating a quite brittle fracture feature. However, the side views of resulting fracture surfaces indicate that the primary particles were elongated along the loading direction (comparing Figure 9b–d), implying that the composite experienced serious plastic deformation during tensile testing, and thus exhibiting a better ductility. This phenomenon was attributed to the softening of the matrix at elevated temperature. In addition, the side views of fracture surfaces indicate that many large-sized cavities nucleated in the SSS, especially around the SiC_p/Al interface (indicated by the arrows in Figure 9c,d). Moreover, both the size and number of the cavities increased as the temperature elevated. It is known that SSS were the weak points of the thixoformed materials because shrinkage porosities and pores always existed in these structures [40]. Meanwhile, its compatible deformation ability was poor due to the existence of hard and fragile eutectics and SiC_p. During tensile testing, the stress concentration was easily generated in the SSS, especially the stress around the SiC_p/Al interface was higher, resulting in the growth of the shrinkage porosities and pores as well as formation of microcracks surrounding the SiC_p/Al interface due to the debonded SiC_p. As the temperature increased, the enhanced plastic deformation ability of the primary particles induced larger stress concentration in the SSS, resulting in the further increased size and number of the cavities. These discontinuous cavities joined together as the loading continued, leading to the fracture of the composite. It was supposed that the large pits on the fracture surface evolved from these cavities and the heaves corresponded to the microstructure surrounding the pits that fractured due to serious deformation, and thus forming the uneven fracture surface. The debonding of SiC_p/Al interface and void nucleation in the matrix contributed to crack initiation and propagation, limiting further increase in ductility for the composite with temperature. Thus, the elongation of the composite exhibited the maximum elongation at 250 °C, but that slightly decreased as the temperature further increased. By comparing Figure 8a–d, the number of the visible SiC_p on the fracture surfaces decreased gradually with increasing the testing temperature, which was evident from the EDS analysis results of elemental Si on the resulting fracture surfaces (Figure 11). The quantitative results indicated that the visible SiC_p fraction decreased from 16.86% to 3.51% as the temperature increased from 25 °C to 300 °C. A decrease in the visible SiC_p fraction was attributed to the increased cavities that facilitated the crack propagation in the matrix. Therefore, the debonding of SiC_p as well as void nucleation and growth were the main fracture mechanisms in the composite at high temperature, and increasing the testing temperature (less than 250 °C) induced relatively improved ductility of the composite, but the elongation decreased when the temperature exceeded 250 °C due to the extensive cavity formation.

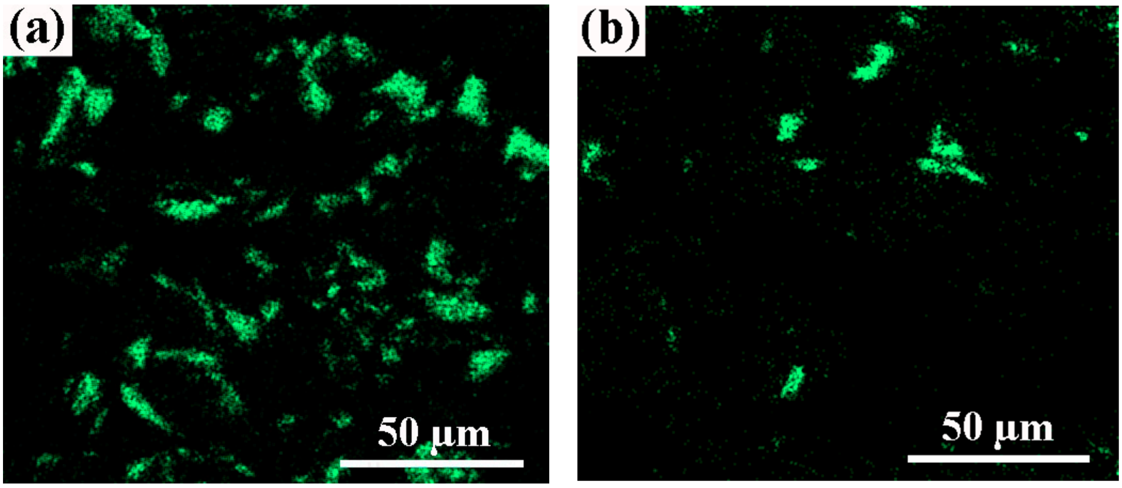

Figure 11. EDS surface scanning analysis of elemental Si on the fracture surfaces of the composite tested at temperatures of (**a**) 25 °C and (**b**) 300 °C.

4. Conclusions

(1) The powder-thixoformed 2024Al/SiC_p composite exhibited outstanding properties and was thereby favorable for prospective applications.

(2) The microstructure of the composite was composed of fine spheroidal primary α-Al particles, intergranular SSS, and SiC_p that were distributed homogeneously in the SSS.

(3) The incorporation of SiC_p to the 2024 alloy brought considerable improvements, the UTS and YS of the PT composite at room temperature were increased by 29.3% and 35%, respectively, compared with the 2024 alloy, which was mainly attributed to the strengthening effects of LTS, TMS, and GNDs.

(4) Owing to the degraded strengthening effects due to the decreased dislocation density and weakened load-bearing ability, the tensile strengths of both the PT materials were all decreased with increasing the temperature, while the composite exhibited higher tensile strength than that of the 2024 alloy at all of the employed testing temperatures, revealing better stability of its strength against temperature over the 2024 alloy.

(5) A high temperature was beneficial for enhancing the ductility of the materials because of the increased softening effect upon increasing the temperatures, whereas the composite possessed the maximum elongation at 250 °C that decreased up to 300 °C because the formation of extensive cavities due to the debonding of the SiC_p/Al interface and fracturing of the matrix limited further increase in ductility as the temperature increased.

(6) The fracture of the composite at room temperature was initiated by failure of the SiC_p, whereas void nucleation and growth as well as debonding between the SiC_p and matrix were the main fracture mechanisms at high temperature.

Acknowledgments: The authors wish to express thanks for the financial support provided by the Basic Scientific Fund of Gansu University (Grant No. G2014-07), the Program for New Century Excellent Talents of the University of China (Grant No, NCET-10-0023), and the Program for Hongliu Outstanding Youth of the Lanzhou University of Technology.

Author Contributions: Pubo Li performed the experiments and wrote the paper under Tijun Chen's guidance, and contributed to all activities.

Conflicts of Interest: The authors declare no conflict of interest.

References

1. Shalaby, E.A.M.; Churyumov, A.Y.; Solonin, A.N.; Lotfy, A. Preparation and characterization of hybrid A359/(SiC + Si_3N_4) composites synthesized by stir/squeeze casting techniques. *Mater. Sci. Eng. A* **2016**, *674*, 18–24. [CrossRef]
2. Cui, Y.; Jin, T.-Z.; Cao, L.-G.; Liu, F.-B. Aging behavior of high volume fraction SiC_p/Al composites fabricated by pressureless infiltration. *J. Alloys Compd.* **2016**, *681*, 233–239. [CrossRef]
3. Ibrahim, I.A.; Mohamed, F.A.; Lavernia, E.J. Particulate reinforced metal matrix composites—A review. *J. Mater. Sci.* **1990**, *26*, 1137–1156. [CrossRef]
4. El-Sabbagh, A.M.; Soliman, M.; Taha, M.A.; Palkowski, H. Effect of rolling and heat treatment on tensile behaviour of wrought Al-SiC_p composites prepared by stir-casting. *J. Mater. Process. Technol.* **2013**, *213*, 1669–1681. [CrossRef]
5. Torralba, J.M.; Costa, C.E.D.; Velasco, F. P/M aluminum matrix composites: An overview. *J. Mater. Process. Technol.* **2003**, *133*, 203–206. [CrossRef]
6. Nadakuduru, V.N.; Zhang, D.L.; Gabbitas, B.; Chiu, Y.L. Tensile properties and fracture behaviour of an ultrafine grained Ti–47Al–2Cr (at.%) alloy at room and elevated temperatures. *J. Mater. Sci.* **2012**, *47*, 1223–1233. [CrossRef]
7. Chen, C.M.; Yang, C.C.; Chao, C.G. Thixocasting of hypereutectic Al–25Si–2.5Cu–1Mg–0.5Mn alloys using densified powder compacts. *Mater. Sci. Eng. A* **2004**, *366*, 183–194. [CrossRef]

8. Jiang, J.-F.; Wang, Y.; Nie, X.; Xiao, G.-F. Microstructure evolution of semisolid billet of nano-sized $SiC_p/7075$ aluminum matrix composite during partial remelting process. *Mater. Des.* **2016**, *96*, 36–43. [CrossRef]
9. Jiang, H.T.; Lu, Y.L.; Huang, W.C.; Li, X.L.; Li, M.Q. Microstructural evolution and mechanical properties of the semisolid Al–4Cu–Mg alloy. *Mater. Charact.* **2003**, *51*, 1–10.
10. Li, P.B.; Chen, T.J.; Zhang, S.Q.; Guan, R.G. Research on semisolid microstructural evolution of 2024 aluminum alloy prepared by powder thixoforming. *Metals* **2015**, *5*, 547–564. [CrossRef]
11. Angers, R.; Krishnadev, M.R.; Tremblay, R.; Corriveau, J.F.; Dubé, D. Characterization of $SiC_p/2024$ aluminum alloy composites prepared by mechanical processing in a low energy ball mill. *Mater. Sci. Eng. A* **1999**, *262*, 9–15. [CrossRef]
12. Xiao, B.L.; Fan, J.Z.; Tian, X.F.; Zhang, W.Y.; Shi, L.K. Hot deformation and processing map of $15\%SiC_p/2009$ Al composite. *J. Mater. Sci.* **2005**, *40*, 5757–5762. [CrossRef]
13. Ezatpour, H.R.; Sajjadi, S.A.; Sabzevar, M.H.; Huang, Y. Investigation of microstructure and mechanical properties of Al6061-nanocomposite fabricated by stir casting. *Mater. Des.* **2014**, *55*, 921–928. [CrossRef]
14. Chen, Y.S.; Chen, T.J.; Zhang, S.Q.; Li, P.B. Effect of ball milling on microstructural evolution during partial remelting of 6061 aluminum alloy prepared by cold-pressing of alloy powders. *Trans. Nonferrous Met. Soc. China* **2015**, *25*, 2113–2121. [CrossRef]
15. Chen, Y.S.; Chen, T.J.; Zhang, S.Q.; Li, P.B. Effects of processing parameters on microstructure and mechanical properties of powder-thixoforged 6061 aluminum alloy. *Trans. Nonferrous Met. Soc. China* **2015**, *25*, 699–712. [CrossRef]
16. Li, P.B.; Chen, T.J.; Qin, H. Effects of mold temperature on the microstructure and tensile properties of $SiC_p/2024$ Al-based composites fabricated via powder thixoforming. *Mater. Des.* **2016**, *112*, 34–45. [CrossRef]
17. Zhang, X.Z.; Chen, T.J.; Qin, Y.H. Effects of solution treatment on tensile properties and strengthening mechanisms of $SiC_p/6061Al$ composites fabricated by powder thixoforming. *Mater. Des.* **2016**, *99*, 182–192. [CrossRef]
18. Li, P.B.; Chen, T.J. Effect of sicp volume fraction on the microstructure and tensile properties of $SiC_p/2024$ Al-based composites prepared by powder thixoforming. *J. Mater. Res.* **2016**, *31*, 2850–2862. [CrossRef]
19. Manson-Whitton, E.D.; Stone, I.C.; Jones, J.R.; Grant, P.S.; Cantor, B. Isothermal grain coarsening of spray formed alloys in the semi-solid state. *Acta Mater.* **2002**, *50*, 2517–2535. [CrossRef]
20. Zoqui, E.J.; Shehata, M.T.; Paes, M.; Kao, V.; Es-Sadiqi, E. Morphological evolution of SSM A356 during partial remelting. *Mater. Sci. Eng. A* **2002**, *325*, 38–53. [CrossRef]
21. Li, P.B.; Chen, T.J.; Qin, H. Effects of pressure on microstructure and mechanical properties of $SiC_p/2024$ Al-based composites fabricated by powder thixoforming. *J. Mater. Sci.* **2017**, *52*, 2045–2059. [CrossRef]
22. Li, P.B.; Chen, T.J.; Ma, Y.; Hao, Y.; Guan, R.G. Microstructural evolution during partial remelting of a 2024 aluminum alloy prepared by cold pressing ball-milled alloy powders. *Mater. Trans.* **2016**, *57*, 91–98. [CrossRef]
23. Fogagnolo, J.B.; Velasco, F.; Robert, M.H.; Torralba, J.M. Effect of mechanical alloying on the morphology, microstructure and properties of aluminium matrix composite powders. *Mater. Sci. Eng. A* **2003**, *342*, 131–143. [CrossRef]
24. Hong, S.J.; Kim, H.M.; Huh, D.; Suryanarayana, C.; Chun, B.S. Effect of clustering on the mechanical properties of SiC particulate-reinforced aluminum alloy 2024 metal matrix composites. *Mater. Sci. Eng. A* **2003**, *347*, 198–204. [CrossRef]
25. Tian, X.F.; Xiao, B.L.; Fan, J.Z.; Wan, Z.Y.; Zuo, T.; Zhang, W.Y. Mechanical properties of nano-SiC_p reinforced 2024 aluminum composite. *Chin. J. Rare Met.* **2005**, *29*, 521–525.
26. Hajjari, E.; Divandari, M. An investigation on the microstructure and tensile properties of direct squeeze cast and gravity die cast 2024 wrought al alloy. *Mater. Des.* **2008**, *29*, 1685–1689. [CrossRef]
27. Nardone, V.C.; Prewo, K.M. On the strength of discontinuous silicon carbide reinforced aluminum composites. *Scr. Metall.* **1986**, *20*, 43–48. [CrossRef]
28. Cheng, N.P.; Zeng, S.M.; Liu, Z.Y. Preparation, microstructures and deformation behavior of $SiC_p/6066Al$ composites produced by pm route. *J. Mater. Process. Technol.* **2008**, *202*, 27–40. [CrossRef]
29. Dai, L.H.; Ling, Z.; Bai, Y.L. Size-dependent inelastic behavior of particle-reinforced metal–matrix composites. *Compos. Sci. Technol.* **2001**, *61*, 1057–1063. [CrossRef]
30. Sekine, H.; Chen, R. A combined microstructure strengthening analysis of SiC_p/Al metal matrix composites. *Composites* **1995**, *26*, 183–188. [CrossRef]

31. Hansen, N. The effect of grain size and strain on the tensile flow stress of aluminium at room temperature. *Acta Metall.* **1977**, *25*, 863–869. [CrossRef]
32. Arsenault, R.J.; Wang, L.; Feng, C.R. Strengthening of composites due to microstructural changes in the matrix. *Acta Metall. Mater.* **1991**, *39*, 47–57. [CrossRef]
33. Edalati, K.; Akama, D.; Nishio, A.; Lee, S.; Yonenaga, Y.; Cubero-Sesin, J.M.; Horita, Z. Influence of dislocation–solute atom interactions and stacking fault energy on grain size of single-phase alloys after severe plastic deformation using high-pressure torsion. *Acta Mater.* **2014**, *69*, 68–77. [CrossRef]
34. Ramakrishnan, N. An analytical study on strengthening of particulate reinforced metal matrix composites. *Acta Mater.* **1996**, *44*, 69–77. [CrossRef]
35. Williamson, G.K.; Hall, W.H. X-ray line broadening from filed aluminum and wolfram. *Acta Metall.* **1953**, *1*, 22–31. [CrossRef]
36. Ungár, T. Dislocation densities, arrangements and character from X-ray diffraction experiments. *Mater. Sci. Eng. A* **2001**, *309–310*, 14–22. [CrossRef]
37. Smallman, R.E.; Westmacott, K.H. Stacking faults in face-centred cubic metals and alloys. *Philos. Mag.* **1957**, *2*, 669–683. [CrossRef]
38. Bailey, J.E.; Hirsch, P.B. The dislocation distribution, flow stress, and stored energy in cold-worked polycrystalline silver. *Philos. Mag.* **1960**, *5*, 485–497. [CrossRef]
39. Ma, K.; Wen, H.; Hu, T.; Topping, T.D.; Isheim, D.; Seidman, D.N.; Lavernia, E.J.; Schoenung, J.M. Mechanical behavior and strengthening mechanisms in ultrafine grain precipitation-strengthened aluminum alloy. *Acta Mater.* **2014**, *62*, 141–155. [CrossRef]
40. Chen, T.J.; Huang, L.K.; Huang, X.F.; Ma, Y.; Hao, Y. Effects of reheating temperature and time on microstructure and tensile properties of thixoforged AZ63 magnesium alloy. *Mater. Sci. Technol.* **2014**, *30*, 96–108. [CrossRef]